# Water-Pillared Sodium Vanadium Bronze Nanowires for Enhanced Rechargeable Magnesium Ion Storage

*Ruimin Sun, Xiao Ji, Chao Luo, Singyuk Hou, Ping Hu, Xiangjun Pu, Longsheng Cao, Liqiang Mai, and Chunsheng Wang\**

**Owing to the advantages of high safety, low cost, high theoretical volumetric capacities, and environmental friendliness, magnesium-ion batteries (MIBs) have more feasibility for large-scale energy storage compared to lithium-ion batteries. However, lack of suitable cathode materials due to sluggish kinetics of magnesium ion is one of the biggest challenges. Herein, water-pillared sodium vanadium bronze nanowires ($Na_2V_6O_{16} \cdot 1.63H_2O$) are reported as cathode material for MIBs, which display high performance in magnesium storage. The hydrated sodium ions provide excellent structural stability. The charge shielding effect of lattice water enables fast $Mg^{2+}$ diffusion. It exhibits high specific capacity of 175 mAh $g^{-1}$, long cycle life (450 cycles), and high coulombic efficiency (≈100%). At high current density of 200 mA $g^{-1}$, the capacity retention is up to 71% even after 450 cycles (compared to the highest capacity), demonstrating excellent long-term cycling performance. The nature of charge storage kinetics is explored. Furthermore, a highly reversible structure change during the electrochemical process is proved by comprehensive electrochemical analysis. The remarkable electrochemical performance makes $Na_2V_6O_{16} \cdot 1.63H_2O$ a promising cathode material for low-cost and safe MIBs.**

## 1. Introduction

Lithium-ion batteries (LIBs) are the most popular energy storage devices in our daily lives owing to their high energy density and long cycling stability.[1,2] However, the safety issue and high cost of lithium (Li) impede further development of LIBs.[3,4] To date, multivalent batteries have captured increasing attention and are promising alternatives for Li-ion batteries.[5–7]

Among them, magnesium ion batteries (MIBs) are especially attractive due to the high safety, low-cost, and high volumetric capacity of magnesium (Mg).[8–11] Different from Li metal, Mg metal is a highly safe anode because of its dendrite-free property during deposition/dissolution process, which effectively avoids the short circuit of MIBs.[12,13] The divalent $Mg^{2+}$ as a charge carrier can achieve a high volumetric capacity of 3833 mAh $cm^{-3}$, which is much higher than that of Li metal (2046 mAh $cm^{-3}$).[14–16] Furthermore, Mg is one of the most abundant elements in the earth's crust (2.9%), while the Li element content is only 0.002%, resulting in a lower cost of MIBs.[6,17,18] Therefore, all these merits make MIBs more promising in the next generation energy storage systems. However, the lack of suitable cathode materials is one of the major challenges for MIBs. The main reason is that the intercalation chemistry of the divalent $Mg^{2+}$ in most cathode materials is much more complicated. The strong interaction between Mg cation and the host lattice leads to sluggish solid-state diffusion and large polarization effect.[19–21] Thus, searching for ideal cathode materials with low Mg diffusion barriers and fast reaction kinetics is a key task for MIBs.

In 2000, Aurbach et al. applied Chevrel phase $Mo_6S_8$ as a cathode material in MIBs and demonstrated a prototype cathode material for high performance MIBs.[22] However, chevrel phase $Mo_6S_8$ shows a low energy density with a low discharge voltage (1.1 V vs $Mg^{2+}/Mg$) and limited theoretical specific capacity (128.8 mAh $g^{-1}$), which restricts its further development in Mg battery. To improve the energy density of MIBs, numerous efforts have been devoted to developing excellent cathode materials. These materials include transition-metal sulfides,[13,14,19] transition-metal oxides,[15,23] and polyanionic compounds,[24,25] and organic compounds. Among them, vanadium-based transition metal oxides with multiple oxidation states can easily achieve electroneutrality, stabilize the crystal structure, lower Mg diffusion barriers, and provide extremely high theoretical capacities during intercalation/deintercalation of multivalent cation.[23,26–29] Moreover, the low cost of vanadium-based oxides has attracted considerable research interests from other battery systems.[30,31] Nowadays, $V_2O_5$ has been widely investigated as a potential cathode material for MIBs.[23,26] Cheng

Dr. R. Sun, Dr. X. Ji, S. Hou, X. Pu, Dr. L. Cao, Prof. C. Wang
Department of Chemical and Biomolecular Engineering
University of Maryland
College Park, MD 20742, USA
E-mail: cswang@umd.edu
Dr. R. Sun, P. Hu, Prof. L. Mai
State Key Laboratory of Advanced Technology for Materials Synthesis and Processing
Wuhan University of Technology
Wuhan 430070, China
Prof. C. Luo
Department of Chemistry and Biochemistry
George Mason University
Fairfax, VA 22030, USA

The ORCID identification number(s) for the author(s) of this article can be found under https://doi.org/10.1002/smll.202000741.

**ADVANCED
SCIENCE NEWS**
www.advancedsciencenews.com

NANO · MICRO
**small**
www.small-journal.com
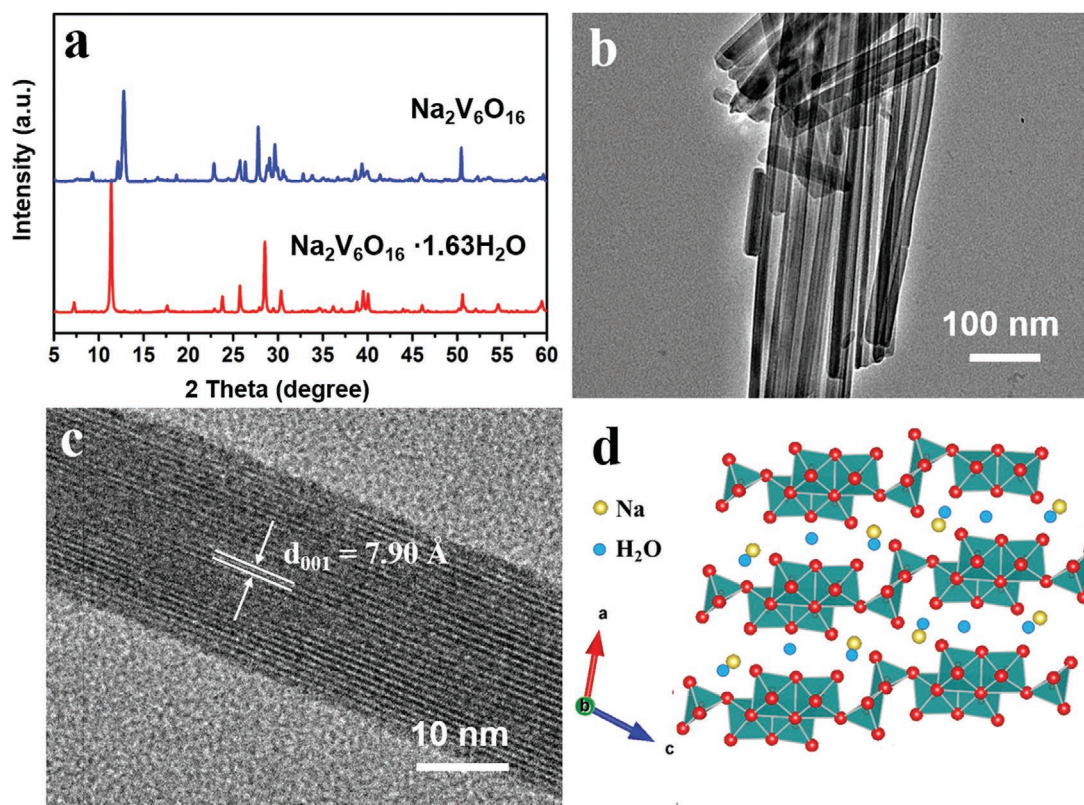
and co-workers studied the Mg storage properties of highly dispersed $V_2O_5$ nanoclusters supported on porous carbon. Using 0.2 M [Mg$_2$(μ-Cl)$_2$(DME)$_4$][AlCl$_4$]$_2$/DME as electrolyte, the composite exhibited a capacitive behavior with an excellent rate performance. The capacity of 100 mAh g$^{-1}$ was maintained even at the high current density of 640 mA g$^{-1}$.[27] $V_2O_5 \cdot nH_2O$ with a bilayer structure also has been researched as cathode for MIBs. Gopalakrishnan and co-workers reported a detailed investigation based on the thermodynamic model with first-principle calculations, revealing the important effect of $H_2O$ during cycling.[26] The large interlayer space in $V_2O_5 \cdot nH_2O$ and "'shielding effect'" of water could shield the strong polarization of Mg cation and facilitate the insertion of Mg$^{2+}$ into the host material.[8,26] In addition, layered vanadium bronzes are also a class of promising cathode materials for MIBs. The interlayer ions in these materials link the layered structure and stabilize the crystal frameworks. Moreover, these materials with large interlayer spacing provide more space for ions storage and diffusion, exhibiting higher specific capacities and long cycling stability.[28] Novak et al. reported the layered vanadium bronzes applied in Mg storage for the first time.[32] In the $V_3O_8$ layer of vanadium bronzes, the zigzag chains composed of $VO_5$ trigonal bipyramids can offer more active sites for the Mg$^{2+}$ insertion.[33] These vanadium bronzes exhibited an initial charge capacity of up to 150 Ah kg$^{-1}$ and retained more than 80 Ah kg$^{-1}$ after 60 deep cycles.[32] Muhammad et al. reported $NaV_3O_8 \cdot 1.69H_2O$ nanobelt as an electrode material for MIBs recently. With all-phenyl complex (APC) electrolyte, the nanobelts exhibited a high specific capacity of 110 mAh g$^{-1}$ at 10 mA g$^{-1}$ after five cycles and 80% capacity retention after 100 cycles at a high current density.[29] However, the electrochemical properties of these materials still remain insufficient to meet the ever increasing demand of energy storage. The low Coulombic efficiency and fast capacity decay still limit the further application of these layered vanadium bronzes. More importantly, the reaction mechanisms of Mg storage in these cathode materials are still unclear.

Herein, we report a novel sodium vanadium bronze $Na_2V_6O_{16} \cdot 1.63H_2O$ cathode for MIBs, which possesses a layered structure for reversible Mg ion intercalation. Interlayer metal ions ($M_xV_nO_m$, M = metal ion) and structural water in this material act as pillars, providing better structural stability and fast ion mobility during cycling. The $Na_2V_6O_{16} \cdot 1.63H_2O$ exhibits an excellent electrochemical performance, in terms of a high specific capacity of 175 mAh g$^{-1}$, long cycle life (450 cycles), and a high coulombic efficiency (≈100%). Even at a high current density of 200 mA g$^{-1}$, a reversible capacity of 65 mA h g$^{-1}$ is obtained and the capacity retention reaches 71% after 450 cycles (compared to the highest capacity), demonstrating excellent long-term cycling performance. The detailed electrochemical kinetic analysis by electrochemical impedance spectroscopy (EIS), galvanostatic intermittent titration technique (GITT) and cyclic voltammetry (CV) further explores the nature of the charge storage. Furthermore, ex situ X-ray diffraction (XRD) and X-ray photoelectron spectroscopy (XPS) analysis were used to clarify the structure change and magnesium storage mechanism during cycling, which confirm the excellent structural reversibility of $Na_2V_6O_{16} \cdot 1.63H_2O$ cathode.

## 2. Results and Discussion

**Figure 1**a shows the XRD patterns of as-prepared samples. All the characteristic peaks can be well indexed to the pure monoclinic $Na_2V_6O_{16} \cdot xH_2O$ phase with a space group of P2/m (JCPDS No. 16-0601). In comparison, the $Na_2V_6O_{16}$ was obtained by annealing $Na_2V_6O_{16} \cdot 1.63H_2O$ at 400 °C for 2 h in argon (Ar) gas. The XRD pattern of $Na_2V_6O_{16}$ is similar with $Na_2V_6O_{16} \cdot 1.63H_2O$. The (001) reflection of $Na_2V_6O_{16}$ shifts to higher $2\theta$ positions (from 11.1° to 12.8°). The reduced lattice space is caused by the removal of the lattice water. According to the thermogravimetric analysis (TGA), the weight percentage of crystalline water can be determined by the weight loss in the temperature range of 100–350 °C. The result shows a weight loss of 4.6 wt% (Figure S1, Supporting Information) and the $x$ value in $Na_2V_6O_{16} \cdot xH_2O$ is calculated to be 1.63. Scanning electron microscopy (SEM) images (Figure S2, Supporting Information) show that the $Na_2V_6O_{16} \cdot 1.63H_2O$ is homogeneous and composed of nanowires with lengths range of 10–40 µm. The widths of the nanowires are in the range of 40–200 nm. The morphology and detailed crystal structure of $Na_2V_6O_{16} \cdot 1.63H_2O$ are further studied by transmission electron microscopy (TEM) (Figure 1b) and high-resolution transmission electron microscopy (HRTEM) (Figure 1c) images. The results confirm the uniformity of $Na_2V_6O_{16} \cdot 1.63H_2O$ nanowires. The HRTEM image reveals the interplanar spacing around 0.79 nm, which matches well with the (001) lattice fringe. SEM images of the $Na_2V_6O_{16}$ nanowires after annealing (Figure S3a, Supporting Information) show that the smooth surface of the origin nanowires was aggregated together with severe breakages. HRTEM (Figure S3b, Supporting Information) image shows that the $Na_2V_6O_{16}$ nanowires have lattice spacing of 0.68 nm. The XPS spectrum (Figure S4a, Supporting Information) shows that $Na_2V_6O_{16}$ contains Na, V and O elements. In the V 2p peaks (Figure S4b, Supporting Information), the two peaks located at 516.8 and 524.1 eV can be assigned to V$^{5+}$,[31,42] indicating that the composition of the material does not change but crystalline water loss after high temperature treatment. The crystal structure of $Na_2V_6O_{16} \cdot 1.63H_2O$ is shown in Figure 1d. The $V_3O_8$ layer consists of $VO_6$ octahedra and edge-sharing $V_2O_8$ pyramid units with sodium ions (Na) in the interlayers.[34] The water via hydrogen-bonding arrangements exists in the non-active sites in the a and b directions, which accommodates additional Mg$^{2+}$ during the electrochemical process.

Coin cells were used to investigate the electrochemical performance of these nanowire cathodes. 0.5 M magnesium bis(trifluoromethane sulfonyl)imide (Mg(TFSI)$_2$) in dimethoxyethane (DME) was used as an electrolyte and activated carbon (AC) clothes were used as the anode. Mg(TFSI)$_2$/DME electrolyte has high oxidation stability and compatibility with most cathodes.[8,23] However, it is not compatible with the Mg metal anode, because of the generation of a passivation layer on the Mg metal anode, which blocks the reversible deposition/dissolution of Mg$^{2+}$.[23] Thus, AC was use as anodes due to its high surface area, which provides sufficient double-layer capacity within the voltage stability window of the electrolyte to match the cathode capacity.[23] The calibrated potential of AC electrode is calculated as 2.4 V versus Mg$^{2+}$/Mg.[35] The cycling performance of the as prepared two

**ADVANCED
SCIENCE NEWS**
www.advancedsciencenews.com

NANO · MICRO
**small**
www.small-journal.com

**Figure 1.** a) XRD patterns of $Na_2V_6O_{16} \cdot 1.63H_2O$ and $Na_2V_6O_{16}$, b) TEM c) HRTEM, and d) crystal structure of $Na_2V_6O_{16} \cdot 1.63H_2O$.

samples ($Na_2V_6O_{16} \cdot 1.63H_2O$ and $Na_2V_6O_{16}$) at a current density of 50 mA g$^{-1}$ is showed in **Figure 2**a. The $Na_2V_6O_{16} \cdot 1.63H_2O$ delivered a high specific capacity of 175 mAh g$^{-1}$, and exhibited the good cycle life with a Coulombic efficiency of nearly 100% during cycling, while $Na_2V_6O_{16}$ obtained a low specific capacity of only 40 mAh g$^{-1}$. The typical charge and discharge curves of the $Na_2V_6O_{16} \cdot 1.63H_2O$ electrode at 50 mA g$^{-1}$ are displayed (Figure S5, Supporting Information). $Na_2V_6O_{16} \cdot 1.63H_2O$ cathodes possess a discharge voltage plateau at around 2.0 V versus $Mg^{2+}$/Mg, which is ascribed to the Mg ion intercalation to the bilayer structure. Rate performance was also measured at progressively increased current densities ranging from 20 to 300 mA g$^{-1}$ (Figure 2b,c). The specific capacity of $Na_2V_6O_{16} \cdot 1.63H_2O$ is 228 mAh g$^{-1}$ at 20 mA g$^{-1}$, and it delivers high capacities of 193, 145, 105, and 91 mA h g$^{-1}$ at current densities of 30, 50, 80, and 100, respectively, demonstrating robust reaction kinetics. Figure 2c displays the discharge-charge curves of $Na_2V_6O_{16} \cdot 1.63H_2O$ at different current densities. Even at a high current density, the cathode still showed good electrochemical properties. At a high current density of 200 mA g$^{-1}$, a capacity of 65 mA h g$^{-1}$ can be obtained and the capacity retention can reach 71% after 450 cycles (compared to the highest capacity), demonstrating excellent long-term cycling performance (Figure 2d). To gain further insights to the reaction kinetics, the EIS tests were conducted (Figure 2e). A compressed semicircle in the high to medium frequency region of each EIS spectrum stands for the charge transfer resistance ($R_{ct}$) of the electrode, and an inclined line in the low frequency range corresponds to the Warburg impendence ($Z_w$).

The charge transfer resistances $R_{ct}$ of the $Na_2V_6O_{16} \cdot 1.63H_2O$ and $Na_2V_6O_{16}$ were determined to be 105 and 206 Ω, respectively, indicating that intercalation of water molecules greatly enhances the conductivity of $Na_2V_6O_{16}$ and guarantees fast ion transfer during the electrochemical process. Therefore, the exceptional electrochemical behaviors of $Na_2V_6O_{16} \cdot 1.63H_2O$ render it as a promising cathode material for MIBs. The electrochemical performance of $Na_2V_6O_{16} \cdot 1.63H_2O$ was also tested in 0.25 м $(PhMgCl)_2/AlCl_3$/THF (APC) and 0.25 м $Mg(TFSI)_2$/ $MgCl_2$/DME (MTCC) electrolytes, which can allow reversible Mg platting/stripping (Figure S6, Supporting Information). However, $Na_2V_6O_{16} \cdot 1.63H_2O$ in these electrolytes delivers low specific capacity. This phenomenon might attribute to the compatibility between Mg and electrolytes, which often occurred in various vanadium oxides.[33] The electrochemical performance of recently reported vanadium-based Mg storage cathode materials are summarized in Table S1, Supporting Information. The $Na_2V_6O_{16} \cdot 1.63H_2O$ in this work stands out among those of MIBs cathodes. On the other hand, specific energy densities of various vanadium-based cathode materials in MIBs are also compared (Figure S7, Supporting Information). The capacities of most vanadium-based MIBs cathodes are under 150 mAh g$^{-1}$ and the average voltages are low, leading to low energy density. The $Na_2V_6O_{16} \cdot 1.63H_2O$ cathode has a high capacity of 230 mAh g$^{-1}$. The specific capacity and average voltage of this material are higher than most of vanadium-based MIBs cathodes, resulting in a high energy density of 460 Wh kg$^{-1}$ (based on the weight of cathode). Although the energy densities of $Li_3V_2(PO_4)_3$[36] and $VO_2$[37] are higher than $Na_2V_6O_{16} \cdot 1.63H_2O$,
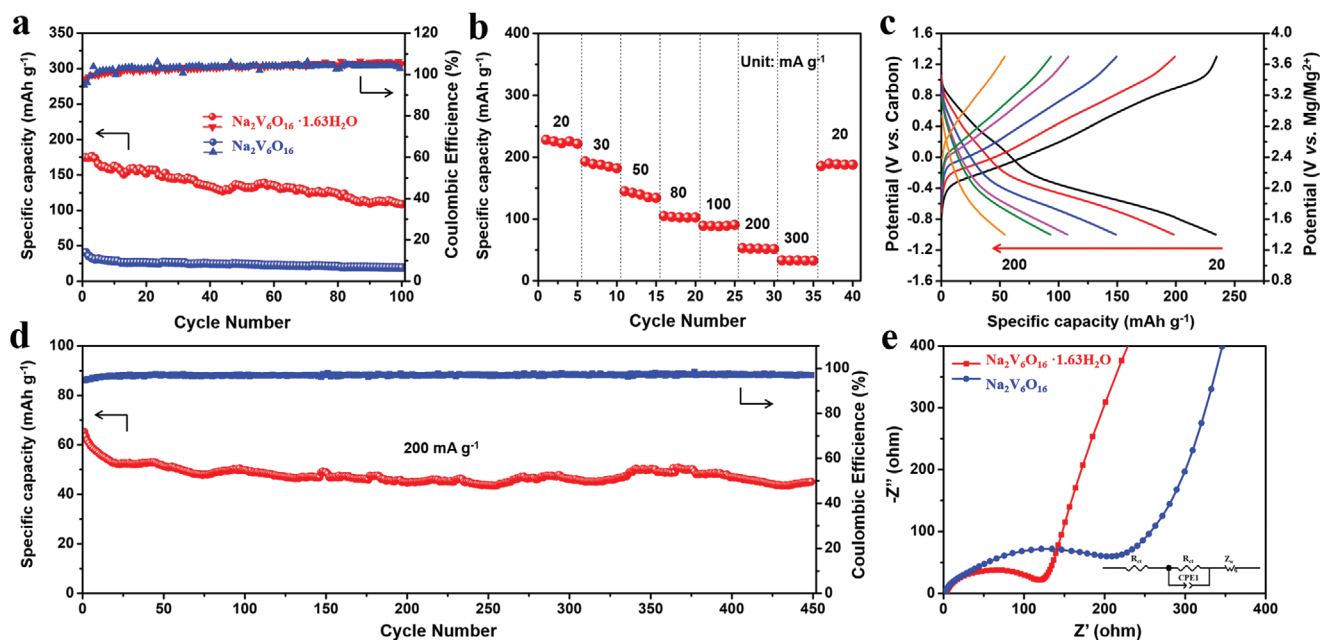
**Figure 2.** a) Cyclic performance of $Na_2V_6O_{16} \cdot 1.63H_2O$ and $Na_2V_6O_{16}$ at a current density of 50 mA g$^{-1}$. b) Rate performance of $Na_2V_6O_{16} \cdot 1.63H_2O$. c) Discharge-charge curves of $Na_2V_6O_{16} \cdot 1.63H_2O$ at different rates. d) Cyclic performance of $Na_2V_6O_{16} \cdot 1.63H_2O$ at a current density of 200 mA g$^{-1}$. e) Nyquist plots of $Na_2V_6O_{16} \cdot 1.63H_2O$ and $Na_2V_6O_{16}$ at the initial state.

their cycling stability and rate capability are much worse than $Na_2V_6O_{16} \cdot 1.63H_2O$ cathode. Taking into account from multiple factors, $Na_2V_6O_{16} \cdot 1.63H_2O$ is one of the most promising candidates among currently studied cathode materials for MIBs.

The kinetic of Mg$^{2+}$ solid-state diffusion in $Na_2V_6O_{16} \cdot 1.63H_2O$ cathode was investigated via GITT (**Figure 3**a).[8,38] $Na_2V_6O_{16} \cdot 1.63H_2O$ cathode delivers a specific capacity of 196 mAh g$^{-1}$ in the voltage range of 1.4 to 3.7 V versus Mg$^{2+}$/Mg, corresponding to 2.3 mol Mg$^{2+}$ intercalation for per mole of $Na_2V_6O_{16} \cdot 1.63H_2O$. Moreover, the Mg$^{2+}$ diffusion coefficient $D^{GITT}$ can be calculated from the potential response to a low constant current pulse (50 mA g$^{-1}$) according to the following equation:[8,38]

$$D^{GITT} = \frac{4}{\pi\tau} \left( \frac{m_B V_M}{M_B S} \right)^2 \left( \frac{\Delta E_s}{\Delta E_\tau} \right)^2 \tag{1}$$

where $\tau$ is the constant current pulse time, $m_B$, $V_M$, $S$, and $M_B$ are the mass, molar volume, electrode-electrolyte interface area, and molar mass of $Na_2V_6O_{16} \cdot 1.63H_2O$, respectively. $\Delta E_S$ is the voltage difference during the open circuit period, and $\Delta E\tau$ represents the total change of cell voltage during a constant current pulse (inset of Figure 3b). Based on the calculated results (Figure 3b), the Mg$^{2+}$ diffusivity of $Na_2V_6O_{16} \cdot 1.63H_2O$ decreases from $4.0 \times 10^{-12}$ to $1.4 \times 10^{-14}$ cm$^2$ s$^{-1}$ during the discharge process due to the increased charge repulsion caused by the increase of Mg$^{2+}$ concentration in the host. It still shows the fast charge transfer kinetics.

The lattice water plays an important role in improving the electrochemical performance of $Na_2V_6O_{16} \cdot 1.63H_2O$. To compare the structural difference between the as-prepared $Na_2V_6O_{16} \cdot 1.63H_2O$ and $Na_2V_6O_{16}$ cathode materials, the Rietveld refinement of XRD patterns of the two samples were

analyzed (Figure S8, Supporting Information). All the XRD peaks of the two samples are indexed to monoclinic structure (JCPDS card No. 16-0601, or JCPDS No. 24-1156), and the fitted lattice parameters of the two samples are listed in Table S2, Supporting Information. As shown in Figure S8c, Supporting Information, both the $Na_2V_6O_{16} \cdot 1.63H_2O$ and $Na_2V_6O_{16}$ have layered structures. The interlayer space of $Na_2V_6O_{16} \cdot 1.63H_2O$ (7.8 Å) is larger than that of $Na_2V_6O_{16}$ (6.8 Å), indicating easier transport and storage for Mg$^{2+}$ in the channel of $Na_2V_6O_{16} \cdot 1.63H_2O$. We also recorded the SEM images of the $Na_2V_6O_{16} \cdot 1.63H_2O$ and $Na_2V_6O_{16}$ electrode after the 1st and 50th cycles (Figure S9, Supporting Information), respectively. The morphology of $Na_2V_6O_{16} \cdot 1.63H_2O$ still maintained well after 50 cycles, while the nanowires of the $Na_2V_6O_{16}$ electrode broke down after only 1 cycle. Given these, the reaction resistance between Mg$^{2+}$ ions and $Na_2V_6O_{16} \cdot 1.63H_2O$ is effectively shielded by the lattice water, resulting in magnesiation with small structural variation due to the pillared effects of the preintercalated water molecules. The large diffusion barrier in $Na_2V_6O_{16}$ hampers the intercalation of Mg ion.

To further explore the nature of the reaction kinetics, CV measurements at various scan rates (0.2 to 1 mV s$^{-1}$) were conducted (Figure 3c). The detailed kinetic analysis was performed regarding that the measured current ($i$) obeys a power law relationship with the scan rate ($v$): $i = av^b$ ($a$, $b$ are adjustable values).[39,40] The $b$-value is determined by the slope of the $\ln(v)$–$\ln(i)$ plots. When the $b$-value approaches to 0.5, the redox reaction is a diffusion-controlled process. If the $b$-value is close to 1.0, the reaction is mostly controlled by the surface-limited capacitive process, including both pseudocapacitance and nonfaradaic double layer contribution.[41] Figure 3d shows that the $b$-values in both cathodic and anodic peaks approach
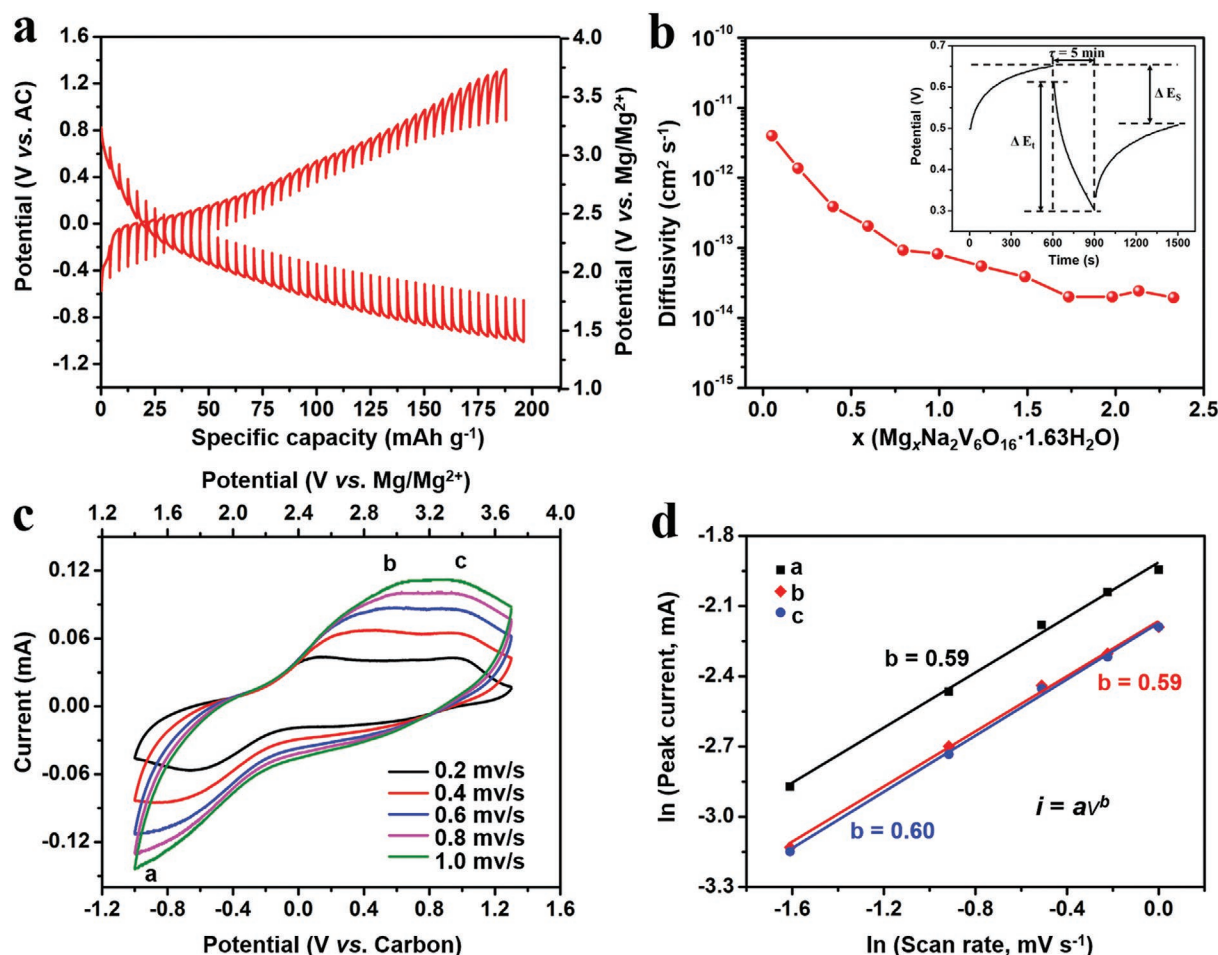
**Figure 3.** a) GITT curve of $Na_2V_6O_{16} \cdot 1.63H_2O$. b) $Mg^{2+}$ diffusivity versus state of discharge (inset: GITT potential response curve with time). c) CV curves of the cell at different sweep rates. d) The relationship of peak current and scan rate for $Na_2V_6O_{16} \cdot 1.63H_2O$.

0.5, demonstrating the reaction kinetics of $Na_2V_6O_{16} \cdot 1.63H_2O$ is determined by Mg ion diffusion process.

To further investigate the charge storage behaviors of the $Na_2V_6O_{16} \cdot 1.63H_2O$ cathode during $Mg^{2+}$ insertion/extraction, ex situ XRD and XPS were performed. **Figure 4**a shows the crystal structure change during electrochemical process. The pristine electrode (state a) shows monoclinic $Na_2V_6O_{16} \cdot 1.63H_2O$ phase. During the discharging process, the (001) reflection shifts slightly to higher $2\theta$ positions. After fully discharged to 1.4 V versus $Mg^{2+}/Mg$ (state d), the interlayer spacing of $Na_2V_6O_{16} \cdot 1.63H_2O$ shrinks from 7.9 to 7.2 A°. The small lattice change is attributed to the strong electrostatic interaction between the intercalated $Mg^{2+}$ and the $(V_3O_8)$-bilayers.[8,31] During the subsequent charge process, the structure can be recovered to $Na_2V_6O_{16} \cdot 1.63H_2O$ with extraction of Mg ion from the interlayer, resulting in a full recovery of the $Na_2V_6O_{16} \cdot 1.63H_2O$. The energy storage mechanism is more evident by exploring the variations of the surface composition and V 2p peaks during the discharge/charge process. The C 1s peak at 284.8 eV in pristine $Na_2V_6O_{16} \cdot 1.63H_2O$ electrode is used as a reference binding energy (Figure S10, Supporting Information). Figure 4b exhibits the Mg 1s core level spectra of $Na_2V_6O_{16} \cdot 1.63H_2O$ in the initial and discharged states (1.4 V vs

$Mg^{2+}/Mg$). No signals for magnesium can be detected in the original $Na_2V_6O_{16} \cdot 1.63H_2O$ electrode. At discharged state, an obvious Mg 1s peak can be observed,[42] confirming the intercalation of $Mg^{2+}$ into $Na_2V_6O_{16} \cdot 1.63H_2O$ phase. Besides, for pristine $Na_2V_6O_{16} \cdot 1.63H_2O$, the peaks located at 516.8, and 524.1 eV are V $2p_{3/2}$ and V $2p_{1/2}$ of $V^{5+}$,[31,42] respectively (Figure 4c). After discharged to 1.4 V versus $Mg^{2+}/Mg$, the V 2p peaks of $V^{5+}$ became weak, while the peaks for $V^{4+}$ appeared at 522.8 and 515.8 eV (Figure 4d).[31] It indicates that partial $V^{5+}$ is reduced to $V^{4+}$ during the $Mg^{2+}$ intercalation process. The most V 2p peaks of $V^{4+}$ can be re-oxidized to $V^{5+}$ when the electrode is at the charged state (Figure 4e). In order to further confirm the $Mg^{2+}$ insertion/extraction mechanism of the cathode material, ex situ transmission electron microscopy energy dispersive spectroscopy (TEM-EDS) elemental mappings of $Na_2V_6O_{16} \cdot 1.63H_2O$ at discharged and charged states were characterized (Figure S11, Supporting Information). The EDS mappings clearly show that Na, V, O are uniformly distributed within the $Na_2V_6O_{16} \cdot 1.63H_2O$ nanowires in both states. In the discharged state, abundant Mg element can be clearly observed within the $Na_2V_6O_{16} \cdot 1.63H_2O$ nanowires, indicating the intercalation of $Mg^{2+}$. In the charged state, only a small quantity of Mg element could be found in the cathode material, demonstrating that $Mg^{2+}$ extraction from
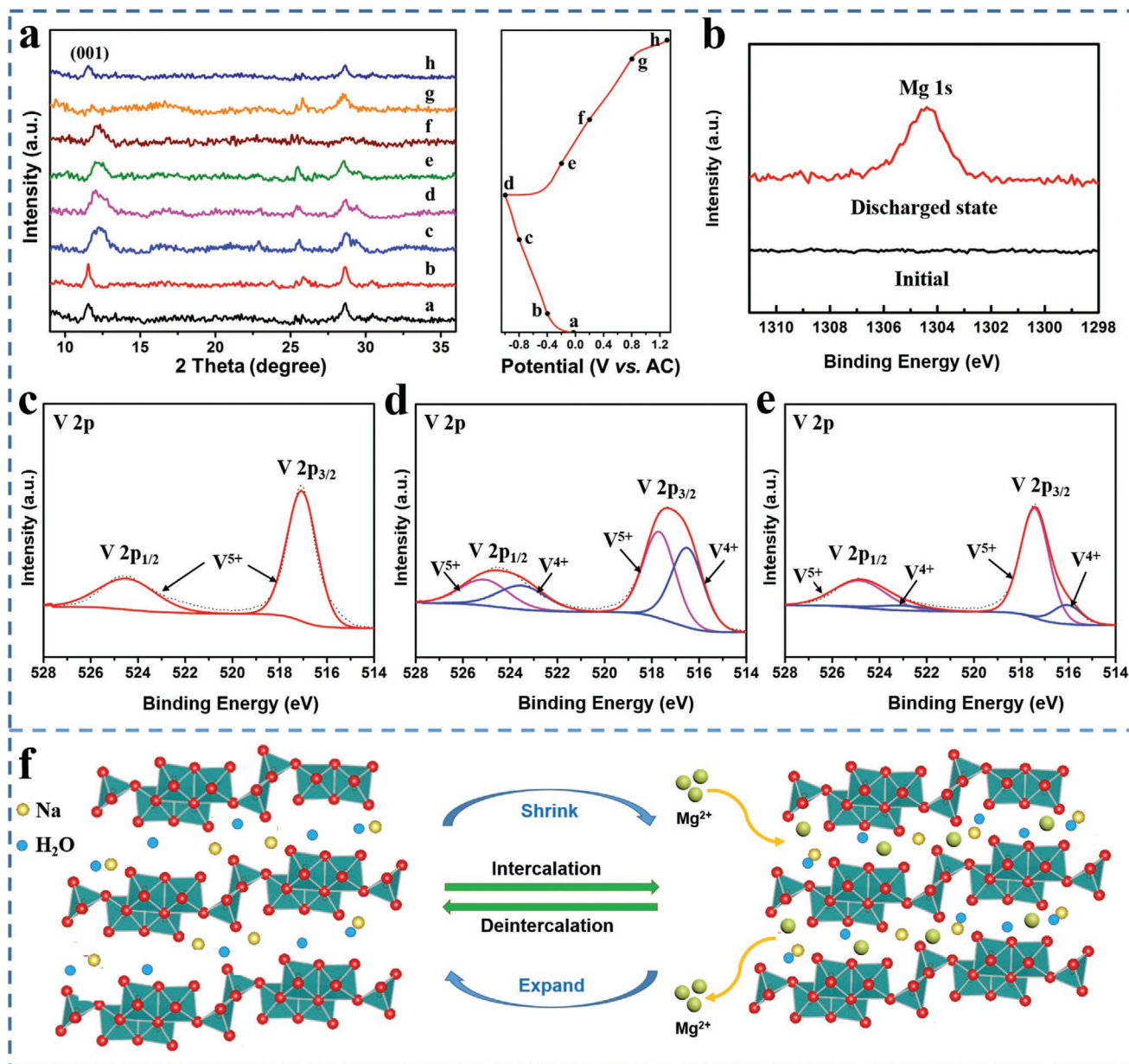
**Figure 4.** Ex situ XRD patterns and XPS spectra of $Na_2V_6O_{16}\cdot1.63H_2O$ collected at different electrochemical states at 50 mA g$^{-1}$. a) Ex situ XRD patterns and corresponding voltage curves (right) during galvanostatic charge and discharge; b) High-resolution Mg 1s spectra at the denoted states; Ex situ V 2p XPS spectra at c) original, d) discharged and e) charged states. f) Schematic illustrations of Mg$^{2+}$ deintercalation and intercalation into $Na_2V_6O_{16}\cdot1.63H_2O$ during electrochemical processes.

the $Na_2V_6O_{16}\cdot1.63H_2O$ nanowires. The mapping results provide more intuitive evidence about the Mg$^{2+}$ insertion/extraction mechanism in $Na_2V_6O_{16}\cdot1.63H_2O$ nanowires. Figure 4f shows the schematic illustration of Mg$^{2+}$ intercalation into and deintercalation from the $Na_2V_6O_{16}\cdot1.63H_2O$ during the electrochemical process. During the discharged process, the Mg$^{2+}$ intercalation is accompanied with the interlayer shrink of the structure. Upon subsequent charge and discharge processes, the Mg$^{2+}$ can reversibly intercalate/deintercalated into the $Na_2V_6O_{16}\cdot1.63H_2O$ layers.

Based on the above results, $Na_2V_6O_{16}\cdot1.63H_2O$ demonstrates the reversible Mg$^{2+}$ insertion/extraction mechanism during the electrochemical process. The overall electrochemical reactions can be described as follows:

$$Overall: Na_2V_6O_{16}\cdot1.63H_2O+2.3Mg^{2+}+4.6e^-$$
$$\leftrightarrow Mg_{2.3}Na_2V_6O_{16}\cdot1.63H_2O \tag{2}$$
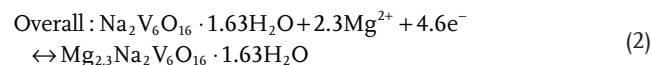
To probe into the discrepancy between $Na_2V_6O_{16}\cdot1.63H_2O$ and $Na_2V_6O_{16}$, first-principle computations based on density functional

**ADVANCED
SCIENCE NEWS**

www.advancedsciencenews.com

NANO · MICRO

**small**

www.small-journal.com
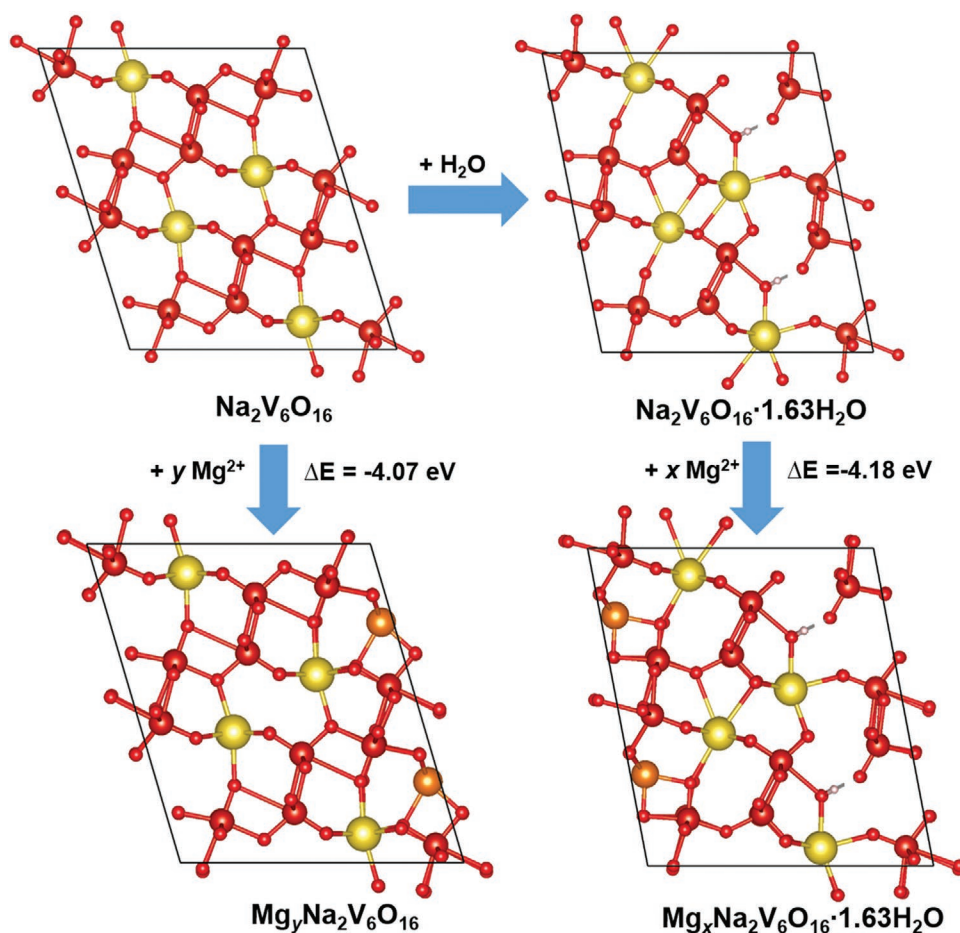
**Figure 5.** The binding energy for $Mg^{2+}$ in $Na_2V_6O_{16} \cdot 1.63H_2O$ and $Na_2V_6O_{16}$ according to DFT calculation. Na: yellow; Mg: orange; V: large size, red; O: small size, red; H: pink.

theory (DFT) were performed to fully understand the role of water in $Na_2V_6O_{16} \cdot 1.63H_2O$ (**Figure 5**). The binding energies between Mg ions in these two structures were calculated. The result shows that introducing water in layers improves the binding energy of $Mg^{2+}$ from 4.07 to 4.18 eV. Therefore, Mg ions are more easily intercalated into $Na_2V_6O_{16} \cdot 1.63H_2O$. Water molecules effectively shield the electrostatic effect between $Mg^{2+}$ and the host lattice, improve the reversibility of magnesium ion intercalation/deintercalation and keep structural stability during cycling.

## 3. Conclusion

In conclusion, a high-performance cathode material, $Na_2V_6O_{16} \cdot 1.63H_2O$, has been developed for MIBs. The one dimensional $Na_2V_6O_{16} \cdot 1.63H_2O$ nanowire cathode delivers a high specific capacity of 175 mAh g$^{-1}$ at 50 mA g$^{-1}$. A capacity of 65 mAh g$^{-1}$ can be achieved at a high rate of 200 mA g$^{-1}$ and the capacity retention can reach 71% after 450 cycles, demonstrating excellent long-term cycle stability. The detailed characterizations and electrochemical kinetic analysis reveal that the charge storage is mainly controlled by the diffusion process. Moreover, according to ex situ XRD and XPS analyses, $Na_2V_6O_{16} \cdot 1.63H_2O$

cathode material possesses a highly stable structure for reversible Mg ion intercalation and deintercalation. It is worth mentioning that the water molecules play an important role in achieving such good electrochemical performance, which act as "'pillars'" to stabilize the layered structure and effectively shield the high charge density of Mg ion. This study demonstrates that $Na_2V_6O_{16} \cdot 1.63H_2O$ is a promising cathode material for magnesium ions storage. More importantly, our findings pave the way for further optimizing the electrochemical properties of layered cathode materials and gain insights to the structure design for developing high-performance inorganic cathodes for Mg storage to meet the requirements of large-scale energy storage.

## 4. Experimental Section

*Materials Synthesis*: The $Na_2V_6O_{16} \cdot 1.63H_2O$ nanowires were synthesized via a simple hydrothermal process.[31] In a typical synthesis, 4 mmol $V_2O_5$ and 4 mmol NaOH were dissolved in 75 mL distilled water. The solution magnetically stirred at room temperature for 1 h. Then the solution was transferred into a Teflon-lined sealed autoclave and heated at 180 °C for 24 h. The obtained suspension was centrifuged and the product was washed thoroughly with distilled water and ethanol several times and then dried at 80 °C in a vacuum oven for 12 h to obtain

$Na_2V_6O_{16} \cdot 1.63H_2O$. For comparison, the $Na_2V_6O_{16}$ was obtained by annealing $Na_2V_6O_{16} \cdot 1.63H_2O$ at 400 °C for 2 h in Ar gas with a heating rate of 2 °C min$^{-1}$.

*Material Characterizations*: Powder XRD (Bruker D8 Advance X-ray diffractometer, Cu K$\alpha$ radiation, $\lambda = 1.5418$ Å) was used to characterize the structure of the samples. SEM (Hitachi SU-70) and TEM and high resolution transmission electron microscopy (HRTEM) (JEOL-2100F) were performed to investigate the morphology and microstructure of the samples. EDS microscope was measured on JEOL-2100F and titan G2 60-300 with image corrector. XPS was conducted on Kratos AXIS 165 X-ray photoelectron spectrometer. XPS peaks were analyzed by CASA software with Shirley background. Before XPS characterization, the cycled electrodes were washed with the corresponding solvents several times to remove residual salts.

*Electrochemical Measurements*: Electrochemical measurements were performed with 2032 coin-type cells in an argon-filled glove box. The working electrode was fabricated on Al foil current collectors. The slurry was obtained by mixing the as prepared materials, acetylene black, and polyvinylidene fluoride (PVDF) binder in a weight ratio of 7:2:1. After drying at 60 °C for 2 h, the electrode was dried in a vacuum oven for 12 h at 100 °C. The average area mass loading was ≈1.5 mg cm$^{-2}$. The glass fiber (GF/A) from Whatman was used as the separator. 0.5 M $Mg(TFSI)_2$ in DME was used as the electrolyte. Mg electrodes can form passivation layer and behave irreversibly in conventional organic electrolyte. Thus, AC cloth was used as the counter electrode due to its high surface area, which guarantees complete charge balance in Mg intercalation process via electrical double-layer capacitance.[8] The standard electrode potential of AC cloth is 0.12 V versus SHE. So its electrode potential was calculated as 2.4 V versus $Mg^{2+}$/Mg. Galvanstatic measurements were performed over a potential range of −1 to 1.3 V versus AC by using a multichannel battery testing system (LAND CT2001A). For batteries used APC or MTCC electrolytes, Mg metal was polished with sandpaper and pushed into disks as anode before use. CV was tested by an electrochemical workstation (CHI 760D). EIS was conducted with Gamry Reference 3000 Potentiostat/Galvanostat/ZRA. The equilibrium (open-circuit) potential of the cells was obtained by GITT, which was carried out at constant current pulses at 50 mA g$^{-1}$ for 5 min, followed by a 10 min relaxation process. The open-circuit-voltage at the end of relaxation was considered to be the thermodynamically equilibrium potential. All of the measurements were carried out at room temperature.

*Computational Details*: All first-principles computations based on DFT[43,44] were performed using the Vienna ab initio Simulation Package (VASP).[45] The Projector Augmented Wave (PAW)[46] method with an energy cut-off of 520 eV was used to describe the ion-electron interaction on a well-converged $k$-point mesh. The Perdew-Burke-Ernzerhof (PBE) functional in the Generalized Gradient Approximation (GGA)[47] was employed to calculate the exchange-correlation energy. A Hubbard U correction of 3.1 eV was added to remove the spurious self-interaction of the vanadium d-electrons as previous works[26] and the DFT-D3[48] was used to correct Van der Waals energy to get accurate interlayer spacing values. The geometry optimizations were performed using the conjugated gradient method, and the convergence threshold was set to be 10$^{-5}$ eV in energy and 0.01 eV Å$^{-1}$ in force. The structure for the water induced and Mg intercalated $Na_2V_6O_{16}$ were proposed based on the DFT energy calculations. The binding energies were calculated by the definition: $E_b = E(Mg_xNa_2V_6O_{16} \cdot nH_2O) - E(Mg_xNa_2V_6O_{16} \cdot nH_2O) - E(Mg)$.

## Supporting Information

Supporting Information is available from the Wiley Online Library or from the author.

## Acknowledgements

## Conflict of Interest

The authors declare no conflict of interest.

## Keywords

[1] K. Liu, Y. Liu, D. Lin, A. Pei, Y. Cui, *Sci. Adv.* **2018**, *4*, eaas9820.

[2] E. A. Olivetti, G. Ceder, G. G. Gaustad, X. Fu, *Joule* **2017**, *1*, 229.

[3] X. Feng, M. Ouyang, X. Liu, L. Lu, Y. Xia, X. He, *Energy Storage Mater.* **2018**, *10*, 246.

[4] R. Sun, Q. Wei, Q. Li, W. Luo, Q. An, J. Sheng, D. Wang, W. Chen, L. Mai, *ACS Appl. Mater. Interfaces* **2015**, *7*, 20902.

[5] M. Mao, T. Gao, S. Hou, C. Wang, *Chem. Soc. Rev.* **2018**, *47*, 8804.

[6] A. Ponrouch, J. Bitenc, R. Dominko, N. Lindahl, P. Johansson, M. Palacin, *Energy Storage Mater.* **2019**, *20*, 253.

[7] P. Canepa, G. Sai Gautam, D. C. Hannah, R. Malik, M. Liu, K. G. Gallagher, K. A. Persson, G. Ceder, *Chem. Rev.* **2017**, *117*, 4287.

[8] Y. Xu, X. Deng, Q. Li, G. Zhang, F. Xiong, S. Tan, Q. Wei, J. Lu, J. Li, Q. An, *Chem* **2019**, *5*, 1194.

[9] Z. Zhang, B. Chen, H. Xu, Z. Cui, S. Dong, A. Du, J. Ma, Q. Wang, X. Zhou, G. Cui, *Adv. Funct. Mater.* **2018**, *28*, 1701718.

[10] J. Lee, I. D. Seymour, A. J. Pell, S. E. Dutton, C. P. Grey, *Phys. Chem. Chem. Phys.* **2017**, *19*, 613.

[11] J. Niu, H. Gao, W. Ma, F. Luo, K. Yin, Z. Peng, Z. Zhang, *Energy Storage Mater.* **2018**, *14*, 351.

[12] M.-Q. Zhao, C. E. Ren, M. Alhabeb, B. Anasori, M. W. Barsoum, Y. Gogotsi, *ACS Appl. Energy Mater.* **2019**, *2*, 1572.

[13] H. D. Yoo, Y. Liang, H. Dong, J. Lin, H. Wang, Y. Liu, L. Ma, T. Wu, Y. Li, Q. Ru, *Nat. Commun.* **2017**, *8*, 339.

[14] X. Xue, R. Chen, C. Yan, P. Zhao, Y. Hu, W. Kong, H. Lin, L. Wang, Z. Jin, *Adv. Energy Mater.* **2019**, *9*, 1900145.

[15] T. Koketsu, J. Ma, B. J. Morgan, M. Body, C. Legein, W. Dachraoui, M. Giannini, A. Demortière, M. Salanne, F. Dardoize, *Nat. Mater.* **2017**, *16*, 1142.

[16] Z. Wang, Y. Zhu, C. Qiao, S. Yang, J. Jia, S. Rafai, X. Ma, S. Wu, F. Ji, C. Cao, *Small* **2019**, *15*, 1902797.

[17] L. P. Wang, Z. Zhao-Karger, F. Klein, J. Chable, T. Braun, A. R. Schür, C. R. Wang, Y. G. Guo, M. Fichtner, *ChemSusChem* **2019**, *12*, 2286.

[18] Y. Zhang, H. Geng, W. Wei, J. Ma, L. Chen, C. C. Li, *Energy Storage Mater.* **2019**, *20*, 118.

[19] K. Liang, K. Marcus, L. Guo, Z. Li, L. Zhou, Y. Li, S. De Oliveira, N. Orlovskaya, Y.-H. Sohn, Y. Yang, *Chem. Commun.* **2017**, *53*, 7608.

[20] Z. Liu, J. Lee, G. Xiang, H. F. Glass, E. N. Keyzer, S. E. Dutton, C. P. Grey, *Chem. Commun.* **2017**, *53*, 743.

ADVANCED
SCIENCE NEWS

www.advancedsciencenews.com

NANO · MICRO

small

www.small-journal.com

[21] K. Shimokawa, T. Atsumi, M. Harada, R. E. Ward, M. Nakayama, Y. Kumagai, F. Oba, N. L. Okamoto, K. Kanamura, T. Ichitsubo, *J. Mater. Chem. A* **2019**, *7*, 12225.

[22] D. Aurbach, Z. Lu, A. Schechter, Y. Gofer, H. Gizbar, R. Turgeman, Y. Cohen, M. Moshkovich, E. Levi, *Nature* **2000**, *407*, 724.

[23] J. L. Andrews, A. Mukherjee, H. D. Yoo, A. Parija, P. M. Marley, S. Fakra, D. Prendergast, J. Cabana, R. F. Klie, S. Banerjee, *Chem* **2018**, *4*, 564.

[24] L. Zhou, Q. Liu, Z. Zhang, K. Zhang, F. Xiong, S. Tan, Q. An, Y. M. Kang, Z. Zhou, L. Mai, *Adv. Mater.* **2018**, *30*, 1801984.

[25] X. Ji, J. Chen, F. Wang, W. Sun, Y. Ruan, L. Miao, J. Jiang, C. Wang, *Nano Lett.* **2018**, *18*, 6441.

[26] G. Sai Gautam, P. Canepa, W. D. Richards, R. Malik, G. Ceder, *Nano Lett.* **2016**, *16*, 2426.

[27] Y. Cheng, Y. Shao, V. Raju, X. Ji, B. L. Mehdi, K. S. Han, M. H. Engelhard, G. Li, N. D. Browning, K. T. Mueller, *Adv. Funct. Mater.* **2016**, *26*, 3446.

[28] E. A. Esparcia Jr., M. S. Chae, J. D. Ocon, S.-T. Hong, *Chem. Mater.* **2018**, *30*, 3690.

[29] M. Rashad, H. Zhang, M. Asif, K. Feng, X. Li, H. Zhang, *ACS Appl. Mater. Interfaces* **2018**, *10*, 4757.

[30] D. Kundu, B. D. Adams, V. Duffort, S. H. Vajargah, L. F. Nazar, *Nat. Energy* **2016**, *1*, 16119.

[31] P. Hu, T. Zhu, X. Wang, X. Wei, M. Yan, J. Li, W. Luo, W. Yang, W. Zhang, L. Zhou, *Nano Lett.* **2018**, *18*, 1758.

[32] P. Novák, W. Scheifele, F. Joho, O. Haas, *J. Electrochem. Soc.* **1995**, *142*, 2544.

[33] H. Tang, F. Xiong, Y. Jiang, C. Pei, S. Tan, W. Yang, M. Li, Q. An, L. Mai, *Nano Energy* **2019**, *58*, 347.

[34] V. Soundharrajan, B. Sambandam, S. Kim, M. H. Alfaruqi, D. Y. Putro, J. Jo, S. Kim, V. Mathew, Y.-K. Sun, J. Kim, *Nano Lett.* **2018**, *18*, 2402.

[35] W. Kaveevivitchai, A. Huq, A. Manthiram, *J. Mater. Chem. A* **2017**, *5*, 2309.

[36] Z. D. Huang, T. Masese, Y. Orikasa, T. Mori, *RSC Adv.* **2015**, *5*, 8598.

[37] T. Luo, Y. Liu, H. Su, R. Xiao, L. Huang, Q. Xiang, Y. Zhou, C. Chen, *Electrochim. Acta* **2018**, *260*, 805.

[38] R. Sun, C. Pei, J. Sheng, D. Wang, L. Wu, S. Liu, Q. An, L. Mai, *Energy Storage Mater.* **2018**, *12*, 61.

[39] C. Luo, G. L. Xu, X. Ji, S. Hou, L. Chen, F. Wang, J. Jiang, Z. Chen, Y. Ren, K. Amine, *Angew. Chem., Int. Ed.* **2018**, *57*, 2879.

[40] R. Sun, S. Liu, Q. Wei, J. Sheng, S. Zhu, Q. An, L. Mai, *Small* **2017**, *13*, 1701744.

[41] R. Sun, Q. Wei, J. Sheng, C. Shi, Q. An, S. Liu, L. Mai, *Nano Energy* **2017**, *35*, 396.

[42] X. Deng, Y. Xu, Q. An, F. Xiong, S. Tan, L. Wu, L. Mai, *J. Mater. Chem. A* **2019**, *7*, 10644.

[43] P. Hohenberg, W. Kohn, *Phys. Rev.* **1964**, *136*, B864.

[44] W. Kohn, L. J. Sham, *Phys. Rev.* **1965**, *140*, A1133.

[45] G. Kresse, J. Hafner, *Phys. Rev. B* **1994**, *49*, 14251.

[46] P. E. Blöchl, *Phys. Rev. B* **1994**, *50*, 17953.

[47] J. P. Perdew, K. Burke, M. Ernzerhof, *Phys. Rev. Lett.* **1996**, *77*, 3865.

[48] S. Grimme, J. Antony, S. Ehrlich, H. Krieg, *J. Chem. Phys.* **2010**, *132*, 154104.